European Journal of Chemistry

View Journal Online
View Article Online

Computational insights into anti-Zika quinazoline compounds: Density functional theory analysis, spectral properties, and molecular dynamics simulations

Akhilesh Kumar Rao and Umesh Yadava *

Department of Physics, Deen Dayal Upadhyaya Gorakhpur University, Gorakhpur, Uttar Pradesh 273009, India

** Corresponding author at: Department of Physics, Deen Dayal Upadhyaya Gorakhpur University, Gorakhpur, Uttar Pradesh 273009, India.*
e-mail: umesh.phy@ddugu.ac.in (U. Yadava).

RESEARCH ARTICLE

10.5155/eurjchem.16.2.207-221.2654

Received: 29 January 2025
Received in revised form: 15 March 2025
Accepted: 9 April 2025
Published online: 30 June 2025
Printed: 30 June 2025

KEYWORDS

DFT
Flavones
Anti-ZIKV
HOMO-LUMO
MD simulation
Molecular docking

ABSTRACT

Zika disease, caused by the Zika virus (ZIKV), a mosquito-borne flavivirus, is a leading factor in the emergence and reemergence of serious illnesses. The compounds *N*-[4-((3-bromo-4-fluorophenyl)amino]-7-methoxyquinazolin-6-yl)-2-butynamide (1), *N*-[4-((4'-6-difluoro-[1,1'-biphenyl]-3-yl)amino)quinazolin-6-yl]-2-butynamide (2), and *N*-[4-((3-fluorophenyl) amino)-7-methoxyquinazolin-6-yl]but-2-ynamide (3) have been reported to exhibit anti-ZIKV activity. In this study, we performed geometry optimizations and structural analysis of these compounds using the B3LYP/6-31G** method. On the basis of the optimized geometries, the electronic properties, infrared (IR) assignments, and thermodynamic parameters were evaluated. The results indicate that these molecules maintain robust conformations in their core rings, with notable variations in the conformations of their side chains and functional groups. It was also observed that the rotational temperatures increase as the rotational constants decrease. The evaluated small HOMO-LUMO energy gaps and molecular electrostatic potential maps suggest high chemical reactivity, indicating ease of intramolecular charge transfer within the molecules. Infrared assignments for normal mode vibrations in the range of 400 to 3800 cm^{-1} were carried out successfully and compared for all three compounds. In addition, to study the structure function, the docking of these molecules along with the control molecule afatinib was performed with the methyltransferase enzyme of the Zika virus. The top-ranked docked complexes were subjected to a molecular dynamics simulation run of 200 ns duration. These theoretical calculations help us to understand how these compounds can interact with enzymes that are involved in the metabolic pathways of the Zika virus.

Cite this: *Eur. J. Chem.* **2025**, *16(2)*, 207-221 **Journal website**: www.eurjchem.com

1. Introduction

Zika virus (ZIKV), a member of the *Flavivirus* genus, is transmitted through the bites of specific *Aedes* mosquito species, including *Aedes luteocephalus*, *Aedes africanus*, *Aedes aegypti*, and *Aedes hensilli* [1]. ZIKV is the main cause of new and re-emerging serious diseases that affect people all over the world [2]. It was first isolated from rhesus monkeys in 1947 [3]. Subsequently, serological evaluations were performed on human serum samples in Uganda, revealing the presence of virus-neutralizing antibodies. It was the first instance of evidence to point to human infection with the Zika virus [4]. Symptoms of a ZIKV infection often include mild fever, conjunctivitis (red eyes), muscle and joint problems, low white blood cell counts, *etc.* [5], but a sizable proportion of persons infected with the virus do not show any signs of disease [6,7]. Serological evidence of the human Zika virus was found in Thailand, Malaysia, Philippines, Tanzania, Egypt and South Asia including India, Bangladesh, Pakistan, Vietnam and Indonesia [8,9]. The World Health Organization declared ZIKV a global health emergency in 2016 due to its rapid spread and its connection to neurological diseases [10]. Many body fluids, including the brain and placental tissues of congenitally infected fetuses, contain ZIKA virus RNA [11]. Reverse transcriptase PCR is a very thorough and explicit approach to ZIKA virus diagnosis [12]. For Zika virus-specific RT-PCR, several conventional and real-time assays concentrating on the structural genes prM, E, *etc.*, and nonstructural genes NS1, NS3, NS4, and NS5 *etc.* have been created [13]. To the best of our knowledge, the FDA has only approved one commercial assay, the Roche Cobas Zika test [14]. Additionally, the FDA has authorized the use of many molecular assays for emergency purposes (EUA), based on RT-PCR [15]. Plasma or serum samples are commonly used for the molecular diagnosis of Zika virus infection in humans within one week of the onset of clinical symptoms [16]. As a result of the longer period of viral shedding in this conveniently obtained collection, urine offers many advantages over serum for the detection of Zika virus RNA. However, exciting studies have shown that pee has a shorter persistence of ZIKV RNA than serum [17]. Currently, there are no particular anti-ZIKV drugs available for the treatment of ZIKV disease in humans. However, there are currently numerous treatments under clinical trials [18].

ISSN 2153-2249 (Print) / ISSN 2153-2257 (Online)
https://dx.doi.org/10.5155/eurjchem.16.2.207-221.2654

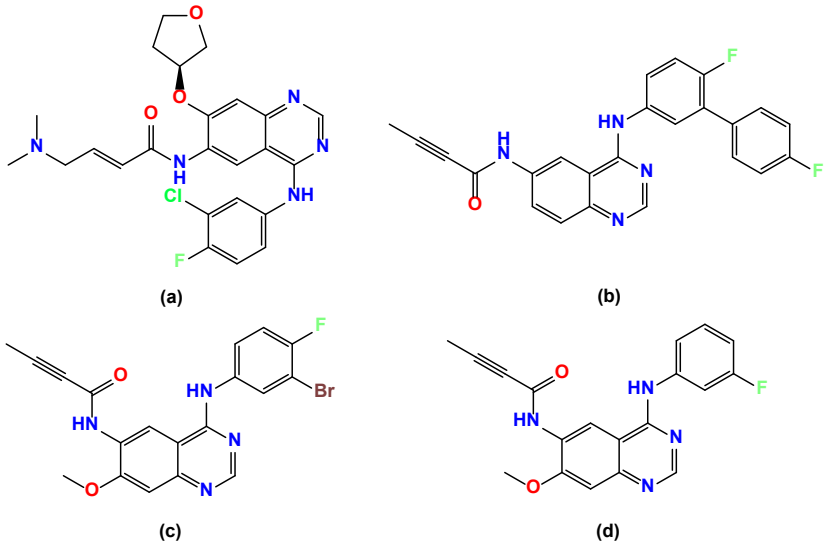

Scheme 1. Chemical structures of compounds (a) afitinib (*N*-[4-[(3-chloro-4-fluorophenyl)amino]-7-[[(3*S*)-tetrahydro-3-furanyl]oxy]-6-quinazolinyl]-4(dimethylamino)-2-butenamide), (b) *N*-(4-((4',6-difluoro-[1,1'-biphenyl]-3-yl)amino)quinazolin-6-yl)-2-butynamide (1) (c) *N*-[4-[(3-bromo-4-fluorophenyl) amino]-7-methoxyquinazolin-6-yl]-2-butynamide (2) and (d) *N*-(4-((3-fluorophenyl)amino)-7-methoxyquinazolin-6-yl)but-2-ynamide (3).

In pursuit of innovative strategies to combat the Zika virus (ZIKV), computational quantum mechanical studies have emerged as a powerful tool that offers unprecedented insight into the molecular intricacies of potential antiviral compounds [19,20]. The urgency to develop effective therapies against ZIKV, known for its association with severe neurological disorders, has led researchers to harness the capabilities of quantum mechanics to unravel the behavior of anti-ZIKV compounds at the atomic and molecular levels [21]. By employing advanced quantum mechanical methodologies, researchers investigate the electronic structure, energetics, and spectroscopic properties of these compounds, aiming to elucidate the underlying mechanisms of their antiviral activity [22].

Experimental observations have demonstrated that tyrosine kinase inhibitors (TKI) exhibit antiflaviviral activities [23]. A series of afatinib derivative tyrosine kinase inhibitor compounds, namely: *N*-[-4((3-bromo-4-flurophenyl)amino]-7-methoxyquinozolin-6-yl]-2-butynamide] (1), *N*-(4-((4′-6-di fluro-[1, 1′-biphenyl]-3-yl)amino)quninazdine-6-yl)-2-butyn amide (2), and *N*-(4((3-flurophenyl) amino)-7-methoxy quinazolil-6-yl)but-2-ynamide (3) have been found endowed with antiviral activities against ZIKV infection *in vitro* and *in vivo* [24]. Afatinib is a quinazoline compound that has a 3-chloro-4-fluoroanilino group at the 4-position, a 4-dimethylamino-trans-but-2-enamido group at the 6-position and an (*S*)-tetrahydro furan-3-yloxy group at the 7-position. The 4-dimethylamino-trans-but-2-enamido group at the 6-position has been replaced by 2-butynamide to obtain compounds 1, 2 and 3. Furthermore, the tetrahydrofuran-3-yloxy group at the 7-position is removed and the 3-chloro-4-fluoroanilino group at the 4-position is replaced by the 4′,6-difluoro-[1,1′-biphenyl]-3-yl group in compound 1. The tetrahydrofuran-3-yloxy group in the 7-position is replaced by the methoxy group in compounds 2 and 3 while the 3-chloro-4-fluoroanilino group at the 4-position is replaced by the 3-fluorophenyl group in compound 2 and by the 3-bromo-4-fluoro-phenyl group in compound 3 (Scheme 1). Compound **3** has shown the highest activity against the ZIKV virus [24]. In the present study, the electronic structure properties, thermodynamic analysis, and IR assignments of compounds 1, 2, and 3 have been investigated and compared. The docking of these molecules and afatinib was performed with the methyltransferase enzyme of the Zika virus, and the best-docked poses were further analyzed using molecular dynamics simulation.

Theoretical calculations, such as geometry optimizations, HOMO-LUMO analysis, and infrared (IR) spectral assignments, play a crucial role in the development of anti-Zika virus (ZIKV) drugs by providing fundamental insights into the molecular properties, reactivity, and stability of potential drug candidates. Here is how these calculations contribute: Molecular Stability and Reactivity. Optimized geometries help determine the most stable conformations of anti-ZIKV quinazoline compounds. Understanding the lengths, angles, and electronic distribution of bonds helps predict interactions with viral proteins or nucleic acids. The energies of HOMO (highest occupied Molecular Orbital) and LUMO (lowest unoccupied Molecular Orbital) indicate the electronic properties of the molecule. A lower HOMO-LUMO gap suggests high reactivity, which may enhance binding to viral targets. Frontier molecular orbital distributions help predict sites for electrophilic and nucleophilic attacks, guiding modifications for improved bioactivity. IR spectral analysis provides characteristic vibrational frequencies, aiding in structural confirmation and comparison with experimental data. The identification of functional groups helps assess interactions with biological targets, such as hydrogen bonding with ZIKV proteins. Molecular descriptors from DFT calculations assist in screening for drug similarity and ADMET (Absorption, Distribution, Metabolism, Excretion, and Toxicity) properties. Molecular docking provides a fast and effective way to predict initial drug-enzyme interactions, while MD simulations refine these predictions by considering dynamic and environmental effects. The combined approach enhances the accuracy of drug design, leading to the development of more effective and specific therapeutics. By integrating these computational approaches, researchers can design more effective anti-ZIKV drugs with optimized electronic and structural properties, reducing the need for costly and time-consuming experimental trials.

2. Experimental

Optimizations of the compounds in their gaseous states were performed using Becke's three-parameter Lee-Yang-Parr (B3LYP) hybrid exchange-correlation functional [25] with the 6-31G** basis set [26], as implemented in the Gaussian03 suite [27].

Table 1. Optimized bond lengths (Å) of the compounds 1, 2, and 3 obtained using the B3LYP/6-31G** method.

Compound 1		Compound 2		Compound 3	
Br1-C15	1.929	C1-C2	1.427	C1-C2	1.427
C2-C6	1.412	C1-C3	1.452	C1-C3	1.446
C2-C20	1.427	C1-C4	1.412	C1-C4	1.417
C2-N39	1.383	C2-C6	1.415	C2-C6	1.412
C3-C20	1.445	C2-N45	1.383	C2-N39	1.383
C3-N39	1.339	C3-N43	1.376	C3-N36	1.376
C3-N39	1.376	C3-C44	1.336	C3-N37	1.339
C4-C11	1.381	C4-C11	1.394	C4-C11	1.381
C4-C20	1.417	C4-H31	1.087	C4-H35	1.085
C4-H32	1.085	C5-C7	1.216	C5-H29	1.088
C5-H22	1.095	C5-C24	1.458	C5-H30	1.094
C5-H30	1.088	C6-C12	1.379	C5-H31	1.095
C5-H31	1.094	C6-H29	1.083	C5-O40	1.456
C5-O40	1.456	C7-C8	1.446	C6-C12	1.383
C6-C12	1.383	C8-N46	1.388	C6-H21	1.081
C6-H23	1.081	C8-O47	1.250	C7-C8	1.458
C7-C8	1.458	C9-C13	1.403	C7-H32	1.096
C7-H33	1.096	C9-C17	1.409	C7-H33	1.096
C7-H34	1.096	C9-N43	1.415	C7-H34	1.096
C7-H35	1.096	C10-H27	1.083	C8-C18	1.215
C8-C18	1.215	C10-N44	1.368	C9-C13	1.405
C9-C13	1.407	C10-N45	1.322	C9-C14	1.412
C9-C14	1.410	C11-C12	1.424	C9-N36	1.412
C9-N37	1.412	C11-N46	1.411	C10-H22	1.083
C10-H24	1.083	C12-H30	1.079	C10-N37	1.365
C10-N36	1.366	C13-C14	1.41	C10-N39	1.324
C10-N39	1.324	C13-H28	1.078	C11-C12	1.431
C11-C12	1.431	C14-C15	1.486	C11-N38	1.424
C11-N38	1.423	C14-C16	1.401	C12-O40	1.373
C12-O40	1.373	C15-C19	1.410	C13-C15	1.389
C13-C15	1.392	C15-C20	1.410	C13-H23	1.078
C13-H25	1.078	C16-C18	1.389	C14-C17	1.394
C14-C17	1.392	C16-F26	1.399	C14-H24	1.086
C14-H26	1.086	C17-C18	1.391	C15-C16	1.389
C15-C16	1.388	C17-H42	1.086	C15-F20	1.393
C16-C17	1.390	C18-H41	1.082	C16-C17	1.400
C16-F21	1.385	C19-C21	1.396	C16-H25	1.082
C17-H27	1.082	C19-H40	1.084	C17-H26	1.084
C18-C19	1.447	C20-C23	1.396	C18-C19	1.448
C19-N38	1.386	C20-H39	1.081	C19-N38	1.386
C19-041	1.246	C21-C22	1.390	C19-O41	1.246
H28-N37	1.008	C21-H38	1.083	H27-N36	1.008
H29-N38	1.010	C22-C23	1.390	H28-N38	1.010
		C22-F25	1.392		
		C23-H37	1.083		
		C24-H34	1.095		
		C25-H35	1.096		
		C24-H36	1.096		
		H32-N43	1.007		
		H33-N46	1.011		

Initial molecular geometries of the compounds were obtained using GaussView software [27], and subsequent optimizations were performed to produce accurate and reliable structures. The absence of imaginary frequencies was ensured for each optimized structure [28]. The optimized parameters were then used for detailed calculations of the electronic structure.

Various molecular properties were investigated, including Mulliken charges, dipole moments, molecular electrostatic potential (MEP) surfaces, infrared (IR) frequencies, highest-occupied to lowest unoccupied molecular orbital (HOMO-LUMO) gaps, and thermodynamic properties of the compounds in their ground states. All calculations were carried out at the B3LYP/6-31G** level of theory, ensuring a consistent and rigorous approach. The study provides valuable insights into the structural and electronic characteristics of the compounds and offers a deeper understanding of their behavior in the gaseous phase. The Mulliken charges and dipole moments shed light on the distribution of charge within the molecules and their overall polarity. Molecular electrostatic potential (MEP) surfaces offer a visual representation of the electrostatic potential, providing insights into the reactivity patterns and potential reaction sites. Furthermore, the investigation includes analysis of infrared frequencies, providing information about vibrational modes and potential spectroscopic signatures. The HOMO-LUMO gaps the compounds' electronic stability and reactivity of the compounds. Furthermore, the thermodynamic properties offer a glimpse into the energy landscape, providing crucial data to understand their stability and behavior under different conditions [29].

The combination of the hybrid functional and the 6-31G** basis set ensures a balanced and accurate description of molecular structures and properties. The comprehensive approach adopted in this study improves our understanding of behavior of the compounds and sets the foundation for future investigations in the field of computational chemistry [19,20]. To investigate the structure-function relationship, standard precision (SP) and extra precision (XP) docking [30] of these antiviral molecules, along with afatinib, was performed within the binding site of the methyltransferase (MTase) enzyme of the Zika virus using the Schrödinger suite [31]. Initially, the 3D structure of the protein (PDB ID: 5XWB) was retrieved from the RCSB website and processed using the PRIME and Protein Preparation Wizard tools [31]. The collected ligands were prepared for docking using the LigPrep module with default parameters. The cocrystallized ligand was used as the center of the binding site, and an electrostatic grid map was generated for each type of atom in the ligands.

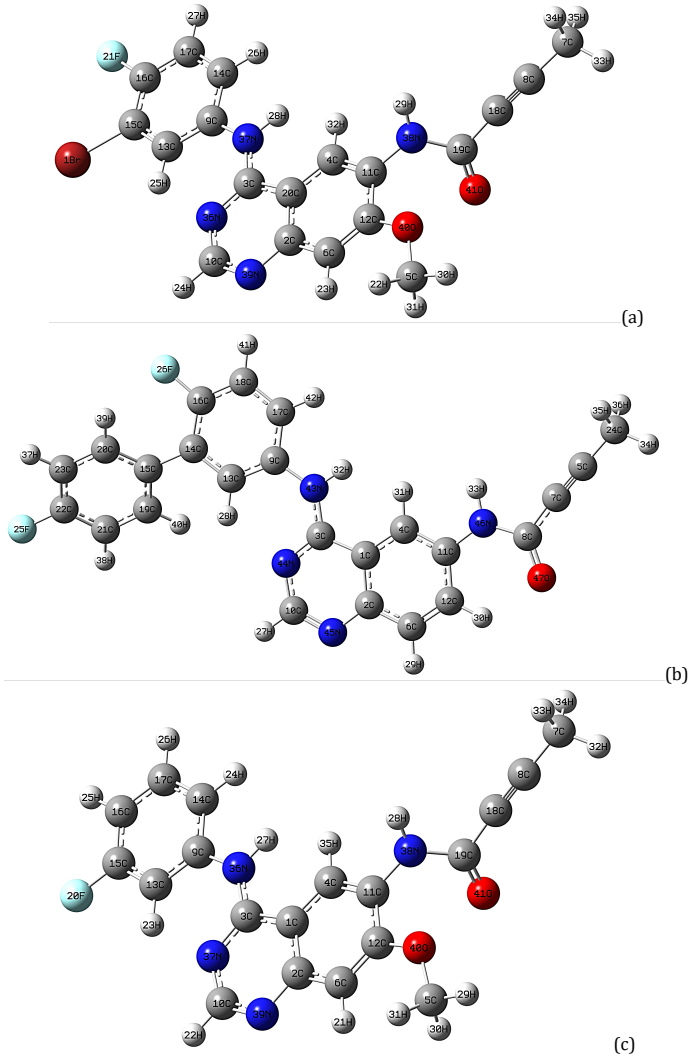

Figure 1. Optimized molecular structures along with the atomic numbering schemes of compounds 1 (a), 2 (b), and 3 (c).

The prepared ligands were then docked within the active site of the MTase using the SP and XP protocols of the GLIDE docking module [31]. The resulting docked poses were further analyzed.

The stability and time evolution of the docked poses were examined using molecular dynamics (MD) simulations of the highest scoring ligand and afatinib over a 200-ns production run using DESMOND-v4.6 [32,33]. The simulation system was set in an orthorhombic box (10×10×10 Å buffer) and solvated with a Monte Carlo-equilibrated periodic SPCE water bath [34]. To mimic physiological conditions, 0.15 M salt was added and the system was neutralized by introducing an appropriate number of sodium and chloride counterions. The energy minimization of the complete system, including protein, ligand, ions and solvents, was carried out using a combination of the steepest descent and limited memory Broyden-Fletcher-Goldfarb-Shanno (LBFGS) algorithms, with a maximum of 2000 iteration steps until reaching a gradient threshold of 25 kcal/mol/Å, according to the default parameters in Desmond [35]. For MD simulation, an anisotropic diagonal position scaling with a 0.002 ps time step was applied to maintain constant pressure. The temperature was set at 300 K, with a 20 ps NPT reassembly under 1 atm pressure, while all other parameters remained at their default values [36]. Finally, each docked complex underwent a 200 ns simulation under similar conditions.

3. Results and discussion

3.1. Molecular geometry optimizations

In Figure 1, we present the optimized structures of compounds 1, 2, and 3, including the corresponding atomic numbering schemes. These structures were calculated using the B3LYP/6-31G** method, providing an accurate representation of the molecular arrangements. Energetic insights into the optimized state of the compounds were obtained through total energy calculations. For compound 1, the total energy was found to be -3773.4235 hartree, while compounds 2 and 3 exhibited total energies of -1418.0981 and -1202.3251 hartree, respectively. These values serve as important indicators of the stability and overall energetics of the compounds studied. The total energy values reported for each compound in its optimized state reflect the energetically favored configurations. Lower total energy values generally correspond to more stable structures, suggesting that compound 1 is probably the most stable among the studied compounds. Further details regarding the geometric parameters of the optimized structures are provided in Tables 1 and 2. These tables offer a comprehensive overview of the key parameters, shedding light on the bond lengths and angles within the molecules.

Table 2. Optimized bond angles (°) of compounds 1, 2, and 3 as obtained using the B3LYP/6-31G** method.

Compound 1		Compound 2		Compound 3	
C6-C2-C20	119.93	C2-C1-C3	115.58	C2-C1-C3	116.00
C6-C2-N39	118.25	C2-C1-C4	118.96	C2-C1-C4	118.32
C20-C2-N39	121.81	C3-C1-C4	125.44	C3-C1-C4	125.66
C20-C3-N36	120.94	C1-C2-C6	118.98	C1-C2-C6	119.93
C20-C3-N37	119.69	C1-C2-N45	122.18	C1-C2-N39	121.84
N36-C3-N37	119.35	C6-C2-N45	118.82	C6-C2-N39	118.22
C11-C4-C20	121.49	C1-C3-N43	119.51	C1-C3-N36	119.70
C11-C4-H32	116.72	C1-C3-N44	120.85	C1-C3-N37	120.87
C20-C4-H32	121.75	N43-C3-N44	119.63	N36-C3-N37	119.42
C22-C5-H30	110.06	C1-C4-C11	121.07	C1-C4-C11	121.50
C22-C5-H31	110.05	C1-C4-H31	120.95	C1-C4-H35	121.73
C22-C5-O40	111.01	C11-C4-H31	117.97	C11-C4-H35	116.74
H30-C5-H31	110.07	C2-C6-C12	121.60	H29-C5-H30	110.07
H30-C5-O40	104.89	C2-C6-H29	117.25	H29-C5-H31	110.05
H31-C5-O40	110.62	C12-C6-H29	121.14	H29-C5-O40	104.91
C2-C6-C12	120.60	C7-C8-N46	113.18	H30-C5-H31	110.03
C2-C6-H23	116.81	C7-C8-O47	122.77	H30-C5-O40	110.63
C12-C6-H23	122.57	N46-C8-O47	124.04	H31-C5-O40	111.02
C8-C7-H33	111.03	C13-C9-C17	119.36	C2-C6-C12	120.60
C8-C7-H34	111.64	C13-C9-N43	124.30	C2-C6-H21	116.79
C8-C7-H35	111.03	C17-C9-N43	116.32	C12-C6-H21	122.58
H33-C7-H34	107.82	H27-C10-N44	115.56	C8-C7-H32	111.03
H33-C7-H35	107.46	H27-C10-N45	117.72	C8-C7-H33	111.63
H34-C7-H35	107.64	N44-C10-N45	126.71	C8-C7-H34	111.04
C13-C9-H14	119.20	C4-C11-C12	119.77	H32-C7-H33	107.82
C13-C9-N37	124.28	C4-C11-N46	117.66	H32-C7-H34	107.47
C14-C9-N37	116.51	C12-C11-N46	122.56	H33-C7-H34	107.64
H24-C10-N36	115.51	C6-C12-C11	119.59	C13-C9-C14	119.40
H24-C10-N39	117.52	C6-C12-H30	121.48	C13-C9-N36	124.16
N36-C10-N39	126.95	C11-C12-H30	118.92	C14-C9-N36	116.43
C4-C11-C12	119.64	C9-C13-C14	121.38	H22-C10-N37	115.51
C4-C11-N38	120.37	C9-C13-H28	118.39	H22-C10-N39	117.48
C12-C11-N38	119.96	C14-C13-H28	120.21	N37-C10-N39	127.00
C6-C12-C11	119.95	C13-C14-C15	119.94	C4-C11-C12	119.65
C6-C12-O40	124.64	C13-C14-C16	116.99	C4-C11-N38	120.39
C11-C12-O40	115.38	C15-C14-C16	123.05	C12-C11-N38	119.93
C9-C13-C15	119.29	C14-C15-C19	119.80	C6-C12-C11	119.95
C9-C13-H25	119.49	C14-C15-C20	121.86	C6-C12-O40	124.63
C15-C13-H25	121.20	C19-C15-C20	118.32	C11-C12-O40	115.40
C9-C14-C17	120.75	C14-C16-C18	122.89	C9-C13-C15	117.92
C9-C14-H26	119.91	C14-C16-F26	120.00	C9-C13-H23	120.65
C17-C14-H26	119.33	C18-C16-F26	117.09	C15-C13-H23	121.42
Br1-C15-C13	119.62	C9-C17-C18	120.14	C9-C14-C17	120.60
Br1-C15-C16	119.41	C9-C17-H42	120.26	C9-C14-H24	119.70
C13-C15-C16	120.96	C18-C17-H42	119.59	C17-C14-H24	119.69
C15-C16-C17	120.43	C16-C18-C17	119.21	C13-C15-C16	124.06
C15-C16-F21	120.75	C16-C18-H41	119.35	C13-C15-F20	117.59
C17-C16-F21	118.81	C17-C18-H41	121.42	C16-C15-F20	118.33
C14-C17-C16	119.35	C15-C19-C21	121.23	C15-C16-C17	117.32
C14-C17-H27	121.24	C15-C19-H40	119.60	C15-C16-H25	120.42
C16-C17-H27	119.39	C21-C19-H40	119.15	C17-C16-H25	122.24
C18-C19-N38	113.81	C15-C20-C23	120.97	C14-C17-H26	120.67
C18-C19-O41	123.43	C15-C20-H39	119.78	C14-C17-H26	119.56
N38-C19-O41	122.73	C23-C20-H39	119.24	C16-C17-H26	119.75
C2-C20-C3	115.98	C19-C21-C22	118.47	C18-C19-N38	113.82
C2-C20-C4	118.34	C19-C21-H38	121.51	C18-C19-O41	123.39
C3-C20-C4	125.66	C22-C21-H38	120.00	N38-C19-O41	122.77
C3-N36-C10	117.97	C21-C22-C23	122.26	C3-N36-C9	131.05
C3-N37-C9	130.92	C21-C22-F25	118.85	C3-N36-H27	115.57
C3-N37-H28	115.55	C23-C22-F25	118.87	C9-N36-H27	113.36
C9-N37-H28	113.51	C20-C23-C22	118.72	C3-N37-C10	118.00
C11-N38-C19	123.14	C20-C23-H37	121.36	C11-N38-C19	123.15
C11-N38-H29	118.89	C22-C23-H37	119.91	C11-N38-H28	118.88
C19-N38-H29	117.84	C5-C24-H34	111.04	C19-N38-H28	117.83
C2-N39-C10	116.32	C5-C24-H35	111.26	C2-N39-C10	116.26
C5-O40-C12	118.95	C5-C24-H36	111.25	C5-O40-C12	118.91
		H34-C24-H35	107.76		
		H34-C24-H36	107.76		
		H35-C24-H36	107.57		
		C3-N43-C9	131.14		
		C3-N43-H32	115.50		
		C9-N43-H32	113.34		
		C3-N44-C10	118.29		
		C2-N45-C10	116.35		
		C8-N46-C11	128.85		
		C8-N46-H33	115.15		
		C11-N46-H33	115.99		

Table 3. Mulliken atomic charges on each atom of compounds 1, 2, and 3.

Compound 1			Compound 2			Compound 3		
Atom no	**Symbol**	**Charge**	**Atom no**	**Symbol**	**Charge**	**Atom no**	**Symbol**	**Charge**
1	Br	-0.094934	1	C	0.101116	1	C	0.091121
2	C	0.219777	2	C	0.221504	2	C	0.219455
3	C	0.535356	3	C	0.529524	3	C	0.533884
4	C	-0.158845	4	C	-0.203510	4	C	-0.159362
5	C	-0.084071	5	C	-0.070126	5	C	-0.083618
6	C	-0.162237	6	C	-0.107119	6	C	-0.16252
7	C	-0.420523	7	C	0.104744	7	C	-0.420485
8	C	-0.090901	8	C	0.489226	8	C	-0.091023
9	C	0.327216	9	C	0.326749	9	C	0.325886
10	C	0.240621	10	C	0.234267	10	C	0.239967
11	C	0.254394	11	C	0.338745	11	C	0.254087
12	C	0.387250	12	C	-0.093607	12	C	0.386920
13	C	-0.080659	13	C	-0.122693	13	C	-0.142248
14	C	-0.143309	14	C	-0.009624	14	C	-0.147195
15	C	-0.032436	15	C	0.071339	15	C	0.348904
16	C	0.348149	16	C	0.305781	16	C	-0.143937
17	C	-0.137509	17	C	-0.146070	17	C	-0.088218
18	C	0.122024	18	C	-0.135024	18	C	0.121566
19	C	0.484567	19	C	-0.112864	19	C	0.485061
20	C	0.091223	20	C	-0.104626	20	F	-0.297993
21	F	-0.277554	21	C	-0.146480	21	H	0.108581
22	H	0.117391	22	C	0.355555	22	H	0.104103
23	H	0.109404	23	C	-0.146864	23	H	0.144197
24	H	0.105769	24	C	-0.421940	24	H	0.074965
25	H	0.156692	25	F	-0.296544	25	H	0.098838
26	H	0.086660	26	F	-0.295673	26	H	0.093937
27	H	0.111503	27	H	0.102794	27	H	0.268955
28	H	0.269073	28	H	0.140339	28	H	0.271241
29	H	0.271429	29	H	0.113324	29	H	0.132900
30	H	0.133568	30	H	0.149051	30	H	0.129247
31	H	0.129565	31	H	0.065717	31	H	0.116957
32	H	0.079047	32	H	0.266425	32	H	0.155609
33	H	0.155969	33	H	0.268550	33	H	0.146699
34	H	0.146896	34	H	0.159594	34	H	0.151613
35	H	0.151927	35	H	0.152253	35	H	0.080085
36	N	-0.534847	36	H	0.152048	36	N	-0.690781
37	N	-0.693148	37	H	0.103417	37	N	-0.531723
38	N	-0.625175	38	H	0.104297	38	N	-0.624968
39	N	-0.509768	39	H	0.102498	39	N	-0.510392
40	O	-0.513892	40	H	0.106251	40	O	-0.514296
41	O	-0.475662	41	H	0.104118	41	O	-0.476019
			42	H	0.080010			
			43	N	-0.692813			
			44	N	-0.530192			
			45	N	-0.499706			
			46	N	-0.634271			
			47	O	-0.479489			

The analysis of these parameters is crucial to understand the structural characteristics and potential reactivity of the compounds. Deviations from standard values or trends in these parameters may indicate structural features relevant to behavior and interactions. The combination of optimized structures, total energy values, and detailed geometric parameters provides a complete picture of the compounds studied. This information is vital to understanding their stability, reactivity, and potential applications in various fields ranging from chemistry to materials science. The data presented establish a foundation for further investigations and applications of these compounds.

3.2. Mulliken charge analyses

Table 3 presents the Mulliken atomic charges for the compounds studied, which were estimated using the density functional theory (DFT) with the B3LYP functional and a 6-31G** basis set. The calculations were conducted in the gaseous phase, offering insights into the distribution of charge among the atoms in each compound. Mulliken atomic charges play a crucial role in understanding the electronic structure and reactivity of molecules [37]. In this study, the DFT/B3LYP method, renowned for its accuracy in describing electronic properties, was used to estimate these charges. The inclusion of the 6-31G** basis set ensures a comprehensive and balanced representation of the electron density around each atom. Positive or negative charges on specific atoms indicate the degree of electron density and, therefore, the electronegativity or electro-positive positivity of those atoms [37]. These insights are essential to predict chemical reactivity, bond polarity, and potential reaction sites within molecules [38]. From Table 3, it has been observed that carbon atoms have partial positive and partial negative charges depending on their positions in the molecules. The highest values of negative charge on carbon atoms are -0.420523, -0.421940, and -0.420485 in compounds 1, 2, and 3, respectively. Hydrogen atoms are partially positively charged while nitrogen and oxygen atoms are partially negatively charged, irrespective of their positions in the molecules. Bromine and fluorine both atoms are partially negatively charged. Fluorine has the highest negative value in compound 3, indicating more electronegativity. This information is particularly relevant for interaction studies.

3.3. HOMO-LUMO analysis

The interaction between the reacting species' lowest unoccupied molecular orbital (LUMO) and highest occupied molecular orbital (HOMO) is what causes an electron to transition, according to the frontier molecular orbital theory (FMO) of chemical reactivity [39]. E_{HOMO} is a quantum chemical characteristic that is frequently linked to a molecule's capacity to donate electrons [40].

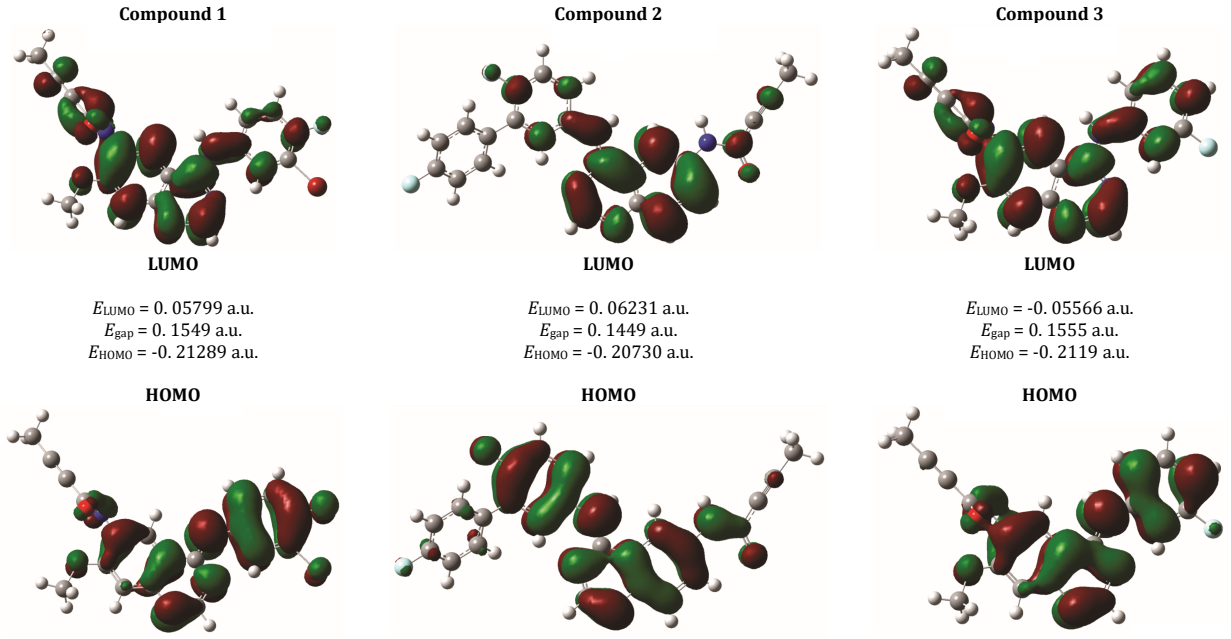

Figure 2. HOMO and LUMO molecular orbitals and their energy values as estimated at the B3LYP/6-31G** level.

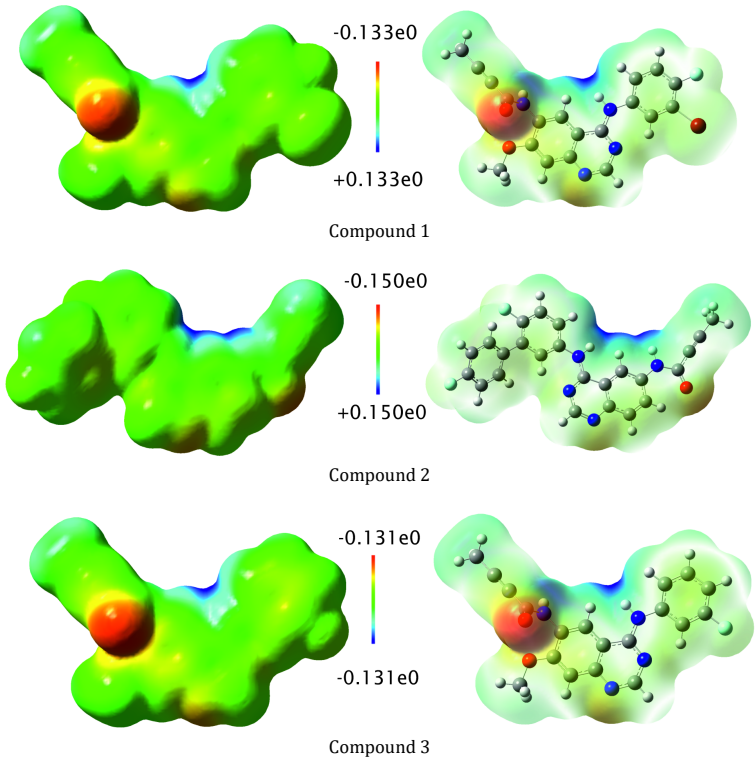

Figure 3. Molecular electrostatic maps of the compounds 1,2 and 3 obtained using the DFT/B3LYP/6-31G** method.

High E_{HOMO} values are probably indicative of a propensity of the molecule to give electrons to suitable acceptor molecules with low empty molecular orbital energies [39,40]. The outermost orbital presumed to contain electrons, HOMO, is thought to operate as an electron donor. On the other hand, LUMO might be considered to be the innermost orbital with open spaces for electrons to enter. Molecular orbitals and their properties are utilized to explain many sorts of reactions and to forecast the most reactive position in conjugated systems. A little frontier orbital gap makes a molecule more polarizable and is typically linked to a high level of chemical reactivity and a poor level of kinetic stability. HOMO and LUMO orbitals and their energy values are shown in Figure 2.

3.4. Molecular electrostatic potential

The molecular electrostatic potential (MEP) is frequently used to understand molecular interactions and as a reactivity, map splaying most probable regions for the electrophilic attack of charged point-like reagents on organic molecules in studies

Table 4. Frequency of the vibration modes, relative intensity and vibrational assignments in the spectra of compound 1.

Frequency (cm^{-1})	IR intensity (km/mol)	Vibrational assignments
17	0.0222	CH_3- Rocking vibration in the plane
134	0.0626	CH_3- Rocking vibration in the plane
143	2.2150	CH_3- Rocking vibration in the plane
177	1.5207	CH_3- Rocking vibration in the plane
203	1.3063	CH_3- Rocking vibration in the plane
210	0.5117	CH_3- Rocking vibration in the plane
279	0.3161	CH_3- Rocking vibration in the plane
455	19.2052	Two benzene rings stretching in a plane
480	7.9702	Single benzene ring vibrates
531	32.6503	Single benzene ring stretching
638	3.3530	Two benzene ring stretching
697	16.8579	Two connected benzene ring stretching
718	18.3474	C=O Out of plane deformation
759	35.6510	C-F stretching of the benzene ring
782	8.3891	N-H stretching of two connected benzene rings
878	32.0762	Stretching in single benzene ring
906	28.3564	C=N stretching in benzene ring
1006	32.0315	O-CH_3 Stretching attached with benzene ring
1017	2.6038	CH_3- Rocking vibration in plane
1022	5.8639	Stretching in a benzene ring attached with fixed O-atom
1047	55.5160	C-CH_3 stretching
1138	4.0690	CH_2- Rocking vibration
1266	36.4754	Stretching in single benzene ring
1304	17.3420	Stretching in single benzene ring
1332	41.3553	C-N stretching attached with two benzene rings
1377	2.2911	C-H_3 Scissoring vibration in the same plane
1407	370.8627	C=N Stretching attached with two benzene ring
1422	171.3653	CH_3- Scissoring vibration
1437	5.7732	CH_3- Rocking vibration
1439	7.3614	CH_2- Scissoring vibration
1455	6.4320	CH_2- Rocking vibration
1458	36.2467	CH_2- Scissoring vibration
1460	906.9779	N-H- Stretching vibration
1466	27.7286	CH_2- Scissoring vibration
1499	294.8916	Scissoring vibration
1524	439.4134	C=N- Stretching two benzene rings attached with each other
1557	205.6282	Stretching in two connected benzene rings
1572	127.5731	Stretching in benzene ring
1597	175.6831	Stretching in single benzene ring
1608	26.0594	Stretching in single benzene ring
1618	164.1261	Stretching in a benzene ring connected with other benzene ring
1718	238.7300	C=O out of plane deformation
2277	135.5385	C≡C Stretching
2932	52.9608	CH_3- Symmetrical vibration
2943	21.2772	CH_3- Symmetrical vibration
3008	6.7612	CH_2- Antisymmetrically vibration
3011	6.1131	CH_3- Antisymmetrically vibration
3062	19.4688	CH_2- Symmetrically vibration

of biological recognition and hydrogen-bonding interactions [41]. It is a highly useful tool for molecular modeling investigations. Predicting potential interactions between various geometries is made simple by MEP. Different colors are used to illustrate the various electrostatic potential levels. Potential growth in the following order: red, orange, yellow, green, and blue. The significance of MEP rests in its ability to dynamically display the molecular size, shape, and regions of positive, negative, and neutral electrostatic potential. MEP is also very helpful in the study of molecular structure and the relationship between it and its physiochemical properties. The MEP map of the compounds is shown in Figure 3. In Figure 3 it has been observed that the negative region is related to electrophilic reactivity (red color), while the positive regions are related to nucleophilic reactivity (blue color). It is evident that the electron densities are very low at the outer surface and near the hydrogen atoms (blue and light blue region), indicating positive electrostatic potentials.

3.5. Infrared spectra

The infrared spectra of the compounds in the range of 400 to 3800 cm^{-1} have been calculated and are presented in Tables 4-6. The calculated IR frequencies have been scaled with a scaling factor of 0.9679 [19,42]. Normal vibrational modes have been assigned on their corresponding vibrational characteristics. Infrared (IR) spectra effectively identify specific functional groups, particularly in larger molecules. The molecules exhibit a syn conformation and structural symmetry, with no imaginary wavenumbers detected, confirming their stability. Vibrational spectroscopy has contributed significantly to understanding the structural and physicochemical properties of crystals and molecular systems. Fundamental vibrations have been systematically assigned on their nature, position, form, and relative intensity. The IR spectra of compounds 1, 2, and 3 within the 400-3800 cm^{-1} range show characteristic vibrational features, including CH and CN stretching modes, among other notable vibrations.

From Table 4, it has been observed that compound 1 exhibits strong N-H stretching (1460 cm^{-1}, 907 km/mol), emphasizing the importance of amine functionalities. C=O out-of-plane deformations are observed at 718 and 1718 cm^{-1} with moderate to high intensities. The diversity of benzene ring vibrations points to a complex aromatic framework. In the spectrum of compound 2, prominent C-N stretching modes (e.g. 1493 cm^{-1}, 585 km/mol) highlight the nitrogen-containing structures. Benzene-ring interactions dominate, with intense vibrations at 1562 cm^{-1} (451 km/mol). Additionally, functional group contributions include C≡C stretching and CH_3 attachments, further diversifying the vibrational spectrum.

Table 5. Frequency of the vibration modes, relative intensity, and vibrational assignments in the spectra of compound 2.

Frequency (cm^{-1})	IR intensity (km/mol)	Vibrational assignments
19	0.0401	CH_3 Rocking vibration in the plane
505	8.9892	Stretching of benzene rings connected with each other
550	9.8547	Stretching of benzene rings connected with each other
567	22.0004	Stretching of a benzene ring connected with C-C
630	3.0919	Stretching of a benzene ring connected with F
655	0.3715	Stretching of two benzene rings connected with each other
679	0.7310	Stretching of two benzene rings connected with C-C
688	4.0338	Stretching of a benzene ring connected with C-C
700	9.7984	C=O Out of plane deformation
747	10.0723	Stretching of two benzene rings connected with each other
769	26.2927	Stretching of a benzene ring connected with F
812	17.0811	Stretching of a benzene ring connected with F
857	37.0474	C-N Out of plane deformation
892	32.0418	Stretching of a benzene ring attached with two nitrogen atoms
998	4.2262	Stretching in benzene ring attached with F
1018	2.8709	Scissoring vibration in the plane
1020	2.1998	Scissoring vibration in the plane
1059	22.6460	C≡C-CH_3 Stretching
1196	79.2316	C-CH_3 Stretching attached with C=O
1267	3.6779	Stretching in a benzene ring attached with -N
1297	2.9408	Stretching in a benzene ring attached with -F
1349	43.9101	Stretching in two benzene rings attached
1377	17.7764	CH_3- Scissoring vibration in the plane
1402	202.5159	Stretching in a benzene ring attached with -F
1435	7.7481	CH_2- Rocking vibration in the plane
1438	7.8824	CH_2- Scissoring vibration in the plane
1485	523.1373	Stretching in a benzene ring attached with another benzene ring
1493	585.6062	C-N Stretching in a benzene ring attached with benzene ring
1508	8.7209	C-N Stretching in a benzene ring attached with C=O
1513	118.7992	Stretching in all four-benzene ring
1535	451.3081	C-N Stretching connected with the benzene ring
1562	170.7172	Stretching in two benzene rings attached to each other
1572	208.7248	Stretching in a benzene ring attached with -F
1583	125.8284	Stretching in a benzene ring attached with -F
1597	163.4928	Stretching in a benzene ring attached with -F
1610	34.8223	Stretching in two benzene rings connected with C-C
1615	26.9603	Stretching in two benzene rings connected with C-C
1624	25.9094	Stretching in a benzene ring attached to another benzene ring
1706	287.5465	C=O Stretching attached with -N
2274	149.0858	C≡C Stretching attached with -CH_3
2944	18.2785	CH_3- Wagging vibration in the plane
3008	5.7120	CH_2- Twisting vibration in the plane
3014	4.9187	CH_2- Twisting vibration in the plane

Table 6. Frequency of the vibrational modes, relative intensity and vibrational assignments in the spectra of compound 3.

Frequency (cm^{-1})	IR intensity (km/mol)	Vibrational assignments
20	0.4986	CH_2- Rocking vibration attached with alkene C
216	0.1326	CH_2- Rocking vibration attached with -O
281	0.0751	CH_2- Rocking vibration attached with -O
345	46.5911	C triple bond C out of plane deformation
353	9.0719	C triple bond C out of plane deformation
510	5.2249	Stretching in benzene ring attached with F
578	17.4487	Stretching in benzene ring attached with F
645	15.2814	Stretching in a benzene ring containing two N
697	14.7333	Stretching in two benzene rings attached to each other
718	20.0948	C=O Out of plane deformation
744	7.2228	Stretching in benzene ring attached with F
882	21.5528	N-H Out of plane deformation
982	3.2651	Stretching in benzene ring attached with F
1007	34.3227	CH_3-O Stretching attached with benzene
1017	2.6013	CH_3- Rocking vibration attached with -C≡C
1022	5.4891	CH_3- Rocking vibration attached with -C≡C
1138	1.6187	CH_2- Rocking vibration attached with -O
1182	1.7246	CH_2- Rocking vibration attached with -O
1189	238.0394	CH_3-C Stretching vibration
1272	87.9545	Stretching in benzene ring attached with F
1318	25.5817	Stretching in benzene ring attached with F
1335	9.9024	Stretching in two benzene rings attached
1339	15.9766	Stretching in benzene ring attached with F
1376	208.6871	CH_3- scissoring vibration attached with C≡C
1377	5.7116	C≡C Scissoring vibration attached with -O40
1437	5.7536	CH_2- Scissoring vibration attached with C≡C
1439	6.8450	CH_2- Scissoring vibration attached with C≡C
1447	246.4877	Stretching in benzene ring attached with F
1455	4.9092	Rocking vibration in the plane
1460	661.1954	CH_2- Scissoring vibration attached with -O40
1466	30.6800	CH_2- Scissoring vibration attached with -O40
1476	7.6803	Stretching in a benzene ring attached with -F
1500	188.7587	Stretching in a benzene ring attached with another benzene ring
1532	441.4520	N36-C3 Stretching attached with the benzene ring

Table 6. (Continued).

Frequency (cm^{-1})	IR intensity (km/mol)	Vibrational assignments
1557	270.9331	Stretching two benzene rings attached
1606	116.6676	Stretching in a benzene ring attached with -F and -N
1613	159.0424	Stretching in a benzene ring attached with -F and -N
1618	128.1936	Stretching in a benzene ring connected with other benzene ring
1717	238.0266	O=C Out of plane deformation
2275	131.8029	C≡C attached with CH_3 wagging vibration attached O40
2943	21.5235	Wagging vibration attached with C≡C
2999	27.7150	Rocking vibration attached with O40
3007	6.8738	CH_2- Twisting out of a plane attached with C≡C
3011	6.2070	CH_2- Twisting out of a plane attached with C≡C

Table 7. Thermodynamic properties of compounds 1, 2 and 3.

Parameters		Compound 1	Compound 2	Compound 3
Rotational temperature (K)		0.01425, 0.00263, 0.00225	0.01444, 0.00233, 0.00202	0.01551, 0.00428, 0.00341
Rotational constant (GHz)		0.29697, 0.05463, 0.04678	0.30091, 0.04848, 0.04209	0.32318, 0.08920, 0.07104
Thermal energy	Translational	44.052	43.954	43.453
(kcal/mol)	Rotational	37.288	37.502	36.305
	Vibrational	100.829	105.930	92.559
	Total	182.169	187.385	172.317
Molecular capacity at volume	Translational	0.889	0.889	0.889
(cal/mol-K)	Rotational	0.889	0.889	0.889
	Vibrational	202.131	234.723	207.470
	Total	203.909	236.500	209.248
Entropy	Traslational	2.981	2.981	2.981
(Cal/mol- K)	Rotational	2.981	2.981	2.981
	Vibrational	85.744	94.392	81.663
	Total	91.000	100.353	87.625
Dipole moment (Debye)		7.3582	7.6266	6.7476
Zero-point vibrational energy (Kcal/mol)		188.16051	219.96177	194.46004

Compound 3 exhibits unique out-of-plane vibrations, such as C≡C stretching (345 and 3537 cm^{-1}, 47 km/mol) and CH_3 wagging (2943 cm^{-1}, 22 km/mol). Intense benzene ring stretches paired with functional groups, such as the vibration at 1557 cm^{-1} (271 km/mol), underscore its distinct structural features. Certain vibrational modes, particularly those involving benzene rings and C-N/C=O bonds, dominate IR absorption. These peaks reflect the significant contribution of these bonds to the compounds' IR profiles. Lower-energy vibrations, such as rocking modes below 500 cm^{-1}, exhibit minimal IR intensities, indicating reduced dipole activity during these motions.

Benzene ring vibrations: All compounds show characteristic stretching vibrations associated with benzene rings, with frequencies ranging from 471 to 1659 cm^{-1}. In particular, the "two-benzene rings stretching" mode exhibits greater intensity in compound 1 (19.2052 km/mol) compared to the others, indicating a more pronounced aromatic interaction.

CH_3 and CH_2 vibrations: Dynamic motions such as rocking, scissoring, and wagging are observed for the methyl (-CH_3) and methylene (-CH_2) groups. For example, CH_2 scissoring in Compound 1 (906.9779 km/mol) and CH_3 scissoring in Compound 3 (246.4877 km/mol) show a high intensity, highlighting their significant contributions to molecular vibrations. This analysis reveals the nuanced vibrational behaviors of each compound, providing insights into their structural and functional properties.

3.6. Thermodynamic properties of compounds 1, 2 and 3

Thermodynamic properties like Zero-point vibration energy, entropy, molecular capacity, *etc.* have been calculated for the molecules by density function theory using B3LYP/6-31G** and are present in Table 7. It is observed that compound 3 exhibits the highest values of rotational temperature and rotational constants among the three, indicating a smaller moment of inertia and a more rigid structure compared to the other compounds. Differences in these parameters suggest variations in molecular geometry and mass distribution. The translational and rotational energies are nearly identical across all compounds, suggesting similar mass and moment of inertia. The vibrational energy varies significantly, with compound 2 having the highest value (105.930 kcal/mol) and compound 3 the lowest (92.559 kcal/mol). It is observed that the translational and rotational contributions remain constant across all compounds. Compound 2 (7.6266 D) has the highest dipole moment, suggesting a stronger polarity, which may influence its solubility and intermolecular interactions. Compound 3 has the lowest dipole moment (6.7476 D), indicating relatively weaker dipole-dipole interactions. Compound 3 has the lowest vibrational energy and entropy, indicating a more rigid structure with lower disorder.

3.7. Global reactivity

DFT has dominated as a sufficient tool for attaining theoretical perceptions of the chemical reactivity and site selectivity. The energy space between HOMO and LUMO is an analytical parameter that governs molecular electrical transport properties. Using HOMO and LUMO energy values for a molecule can describe global chemical parameter descriptors of molecules, such as electron affinity (A), ionization potential (I), global hardness (η), Softness (S), Electronegativity (χ), Chemical potential (μ) and Electrophilicity Index (ω) have been analyzed of the compounds. On account of HOMO energy and LUMO energy, the above are calculated using the below equations. By Koopmans's theorem for closed-shell molecules, there are following global parameters, which can be calculated as [42,43]:

$$\text{Global hardness } (\eta) = \frac{I - A}{2} \quad (1)$$

$$\text{Softness } (S) = \frac{1}{2\eta} \quad (2)$$

$$\text{Electronegativity } (\chi) = \frac{I + A}{2} \quad (3)$$

$$\text{Chemical potential } (\mu) = \frac{-(I + A)}{2} \quad (4)$$

$$\text{Electrophilicity index } (\omega) = \frac{\mu^2}{2\eta} \quad (5)$$

where A and the I are the electron affinity and ionization potential of the given molecules.

Table 8. The calculated global reactivity parameters of the molecules.

Parameters	Compound 1	Compound 2	Compound 3
Energy (HOMO) Hartree	-0.21289	-0.20730	-0.21119
Energy (LUMO) Hartree	-0.05799	-0.06231	-0.05566
Δ*E* Hartree	0.15490	0.14499	0.15553
Global hardness (η) Hartree	0.0774	0.0725	0.0778
Softness (S) Hartree^{-1}	6.4558	6.8961	6.4296
Electronegativity (χ) Hartree	0.1354	0.1348	0.1334
Chemical potential (μ) Hartree	-0.1354	-0.1348	-0.1334
Electrophilicity index (ω) Hartree	0.1184	0.1253	0.1145
Electron affinity (A) Hartree	0.0580	0.0623	0.0557
Ionization potential (I) Hartree	0.2129	0.2073	0.2112

Table 9. Various energy terms (kcal/mol) as obtained through the SP and XP docking of molecules within the binding site of methyltransferase.

Rank (SP)	Compound	GScore	HBond	vdW	Coul	Emodel	CvdW
1	Compound 3	-5.07	-0.4	-37.6	-6.0	-55.0	-43.6
2	Afatinib	-4.64	-0.4	-38.6	-12.7	-69.1	-51.3
3	Compound 1	-4.29	-0.4	-36.4	-5.6	-54.4	-41.9
4	Compound 2	-3.64	-0.1	-42.3	-5.1	-56.9	-47.4
Rank (XP)	**Compound**	**GScore**	**HBond**	**vdW**	**Coul**	**Emodel**	**CvdW**
1	Afatinib	-6.36	-1.2	-41.4	-9.1	-72.7	-50.6
2	Compound 3	-4.68	-0.7	-42.0	0.6	-61.9	-41.3
3	Compound 1	-4.61	-0.7	-41.4	-4.5	-61.6	-45.9
4	Compound 2	-2.61	-0.7	-40.5	-1.0	-57.9	-41.5

All determined values of HOMO energy, LUMO energy, energy gap, hardness, softness, electronegativity, chemical potential, electrophilicity index, electron affinity, and ionization potential are shown in Table 8.

Compound 3 shows the least amount of HOMO-LUMO energy gap ΔE_{gap} = 0.02532 Hartree, indicating it is the most delicate molecule. The molecule that has the highest HOMO energy is compound 3 (E_{HOMO} = 0.21119Hartree). It represents that it can be the best electron acceptor. These two properties, potential ionization (I) and affinity (A), are so important that they decide to calculate the global hardness (η) and electronegativity (χ). HOMO and LUMO are concerned with an electro-orbital potential. Compound 2 (I = 0.2073 Hartree) has the least potential ionization, which will make it a better electron donor. Compound 3 has the best affinity (A = 0.0557 Hartree), as a result, it is the best electron acceptor. The chemical reactivity changes with the activity of the molecule. Compound 3 has a global hardness value (η = 0.0778 Hartree) that is less in all molecules. Thus, compound 3 is found with more activity in comparison to other compounds. Compound 3 electronegativity value (χ = 0.1334 Hartree) is higher than other compounds that is the compound is the best electron acceptor. Value for ω for compound 3 (ω = 0.1145 Hartree) shows that they are more powerful in electrophiles compared to others. Compound 3 has fewer frontiers orbital gaps, hence, it is more polarized and it is associated with less kinetic stability and higher chemical reactivity and hence can be said a soft molecule [34].

3.8. Docking and binding pose analysis

The SP and XP docking of compounds 1, 2, 3, and afatinib was carried out within the binding site of the MTase enzyme (PDB ID: 5WXB) of the Zika virus, and the results are presented in Figures 4a and b, and Table 9. From Table 9, it is observed that compound 3 exhibits the highest docking score (-5.07 kcal/mol), followed by afatinib (-4.64 kcal/mol). Compounds 1 and 2 rank third and fourth, respectively, in agreement with their experimentally observed inhibitory activities [24]. The Emodel energies follow the same trend, except for afatinib and compound 3, which are reversed in ranking. The XP docking results provide a clearer differentiation of molecular affinities. The XP docking score of afatinib (-6.36 kcal/mol) is better than that of compound 3 (-4.68 kcal/mol), followed by compounds 1 and 2 (Table 9). The Emodel energies also follow the same order. Furthermore, it is concluded that the van der Waals energy component plays a major role in the interaction of these molecules within the binding site of the MTase enzyme of the Zika virus.

Figures 4a and 4b illustrate the hydrogen bonding and other noncovalent interactions obtained through SP and XP docking, respectively. Compound 3 forms hydrogen bonds with residues GLY148, LYS105, and THR104, while afatinib interacts by hydrogen bonding with GLU149 and GLU111. Hydrophobic interactions are observed with CYS82, TYR103, VAL130, VAL132, PHE133, and ILE147, among others. SER150, THR104, and HIS110 contribute to polar interactions, while LYS182, ARG84, ARG163, and ARG160 exhibit positively charged interactions, and GLU149, ASP146, GLU111, and ASP131 display negatively charged interactions. In Figure 4b, it can be observed that afatinib forms hydrogen bonds with GLU111, LYS105, ARG163, and GLY148, while compound L3 interacts with GLY81 and GLY148. Hydrophobic interactions are contributed by TRP87, CYS82, VAL130, VAL132, PHE133, TYR103, and ILE147. Polar interactions arise due to SER88, SER56, THR104, and HIS110, while positively charged interactions are exhibited by LYS182, ARG84, ARG183, and LYS105, and negatively charged interactions are observed with GLU149, ASP146, GLU111, ASP131, and ASP79. Based on docking scores, hydrogen bonding, and other noncovalent interactions, afatinib and compound 3 demonstrate stronger interactions compared to compounds 1 and 2.

3.9. Explicit solvent molecular dynamics simulation analysis

Molecular dynamics (MD) simulations were performed on the best-docked poses of the afatinib-MTase and Compound 3@MTase complexes using the SPC/E water model, salts; and sodium ions within the improved OPLS4 force field environment [44]. Following MD simulations, various thermodynamic parameters were evaluated, including the root mean square deviations (RMSD) of heavy atoms and the root mean square fluctuations (RMSFs) of the residues. Additionally, noncovalent interactions during the simulations were analyzed. The RMSD plots of protein C-α atoms and ligand atoms for afatinib and molecule 3 over a simulation period of 200 ns are shown in Figures 5a and 5b, respectively. As seen in Figure 5a, the protein RMSD stabilizes at an average value of 2.1 Å within the first 20 ns, remaining constant with minor fluctuations for the rest of the simulation. The RMSD of afatinib fluctuates up to 118 ns, after which it stabilizes at 14 Å within the MTase binding site of the Zika virus, suggesting that a new binding site is achieved during the simulation.

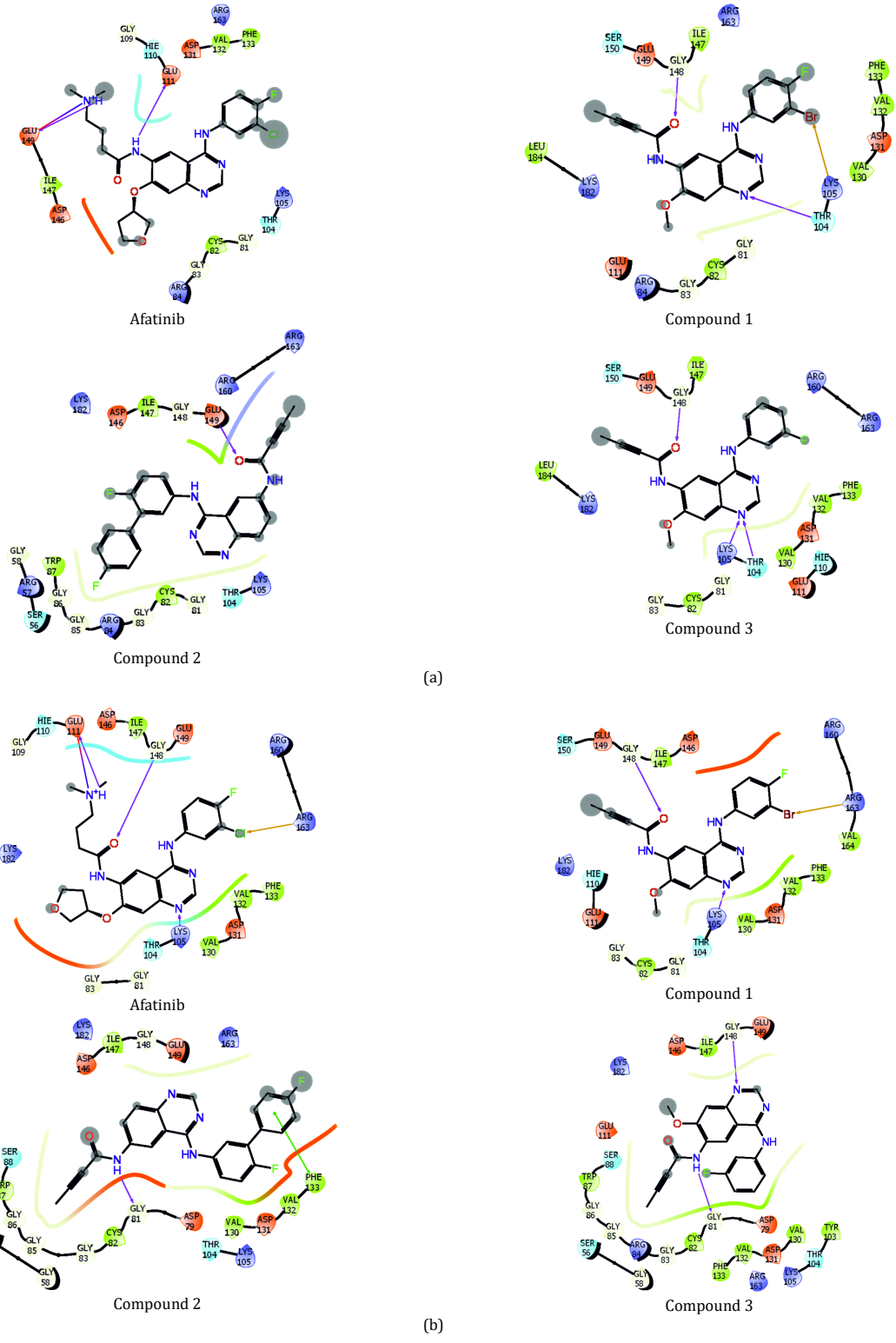

Figure 4. Hydrogen bonding and other noncovalent interactions as obtained through (a) standard-precision (SP) docking and (b) extra-precision (XP) docking.

For the Compound 3@MTase complex (Figure 5b), the protein C-α RMSD increases with simulation time, reaching an average deviation of 2.8 Å at 100 ns, after which it remains stable with slight fluctuations. Unlike afatinib, compound 3 attains its equilibrium conformation within the binding site at an early stage (20 ns). The average RMSD of compound 3 within the binding site remains approximately 5.6 Å, indicating that the ligand remains within the same binding site throughout the simulation.

The root mean square fluctuation (RMSF) plots for the Afatinib@MTase and Compound 3@MTase complexes are presented in Figures 5c and 5d, respectively. These plots provide information on local conformational changes along the protein chain.

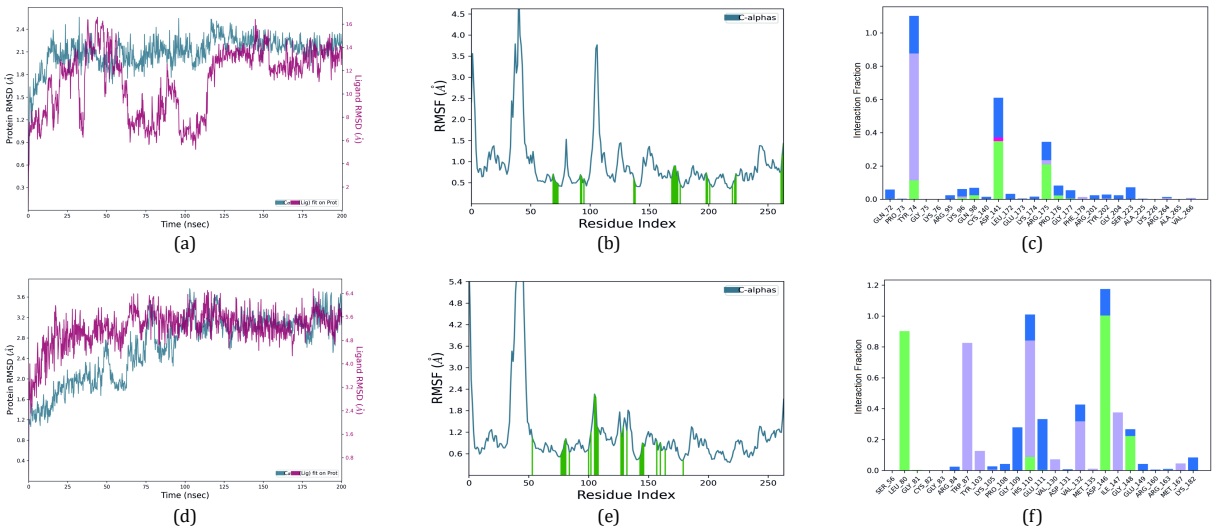

Figure 5. Results of the MD simulation (a) Variation of the RMSD of protein C-α and the afatinib molecule during the molecular dynamics simulation run of 200 ns. (b) Variation of the RMSD of the protein C-α and compound 3 molecules during the simulation of molecular dynamics of 200 ns. (c) RMSF of the interacting protein residues in the Afatinib@MTase complex. (d) RMSF of the interacting protein residues in Compound 3@MTase complex, (e) Interactions fraction of hydrogen bonds, hydrophobic, ionic, and water bridges during MD simulation of the interacting residues in Afatinib@MTase complex, (f) Interactions fraction of hydrogen bonds, hydrophobic, ionic and water bridges during MD simulation of the interacting residues in Compound 3@MTase complex.

The peaks indicate the regions of the protein that exhibit the highest fluctuations. In Figure 5a, significant fluctuations are observed in residues 1-50 and 100-110, while other regions show relatively lower fluctuations. In contrast, Figure 5b shows that the RMSF values for residues 1-50 in the Compound 3@MTase complex are higher than those observed in the afatinib-bound system, indicating greater flexibility in this region. Both simulations reveal relatively stable regions with RMSF values below 1.5 Å for most of the protein, suggesting structural rigidity in these segments. However, the RMSF plot for compound 3 exhibits more pronounced fluctuations across multiple regions, implying that the protein undergoes greater conformational changes compared to the afatinib-bound system. The green bars in both plots mark key interaction sites. Variations in the number and intensity of these interaction sites suggest potential differences in the stability of the ligand and binding interactions during the simulations. Additionally, differences in interaction site distribution indicate that the ligands may induce distinct effects on protein flexibility.

The histograms shown in Figures 5e and 5f illustrate the protein-ligand interaction frequencies during molecular dynamics simulations for the Afatinib@MTase and Compound 3@MTase complexes, respectively. The first histogram (Afatinib@MTase), Figure 5e, shows dominant interactions at residues TYR74, GLY75, and LEU141, with a mix of hydrogen-bonding, hydrophobic, and water-bridge interactions. The second histogram (Compound 3@MTase) presents more dispersed interactions, with strong contributions from SER56, GLY81, GLU111, ASP146, and GLU149. It can be seen that Afatinib forms stable interactions with residues located primarily in a concentrated region, particularly around LEU141 and TYR74. Compound 3, however, engages with a broader range of residues, suggesting a more dynamic binding mode. In both cases, specific residues exhibit almost 100% interaction fractions, indicating consistent ligand binding during simulation. Compound 3 forms more extensive polar and charged interactions (*e.g.*, GLU111, ASP146, GLU149), which could influence binding stability. Although both ligands exhibit strong interactions with MTase, Afatinib appears to maintain a more rigid and specific binding profile, while Compound 3 shows broader residue engagement, potentially allowing more flexibility at the binding site. These differences could impact their respective binding affinities and functional effects.

4. Conclusions

In summary, the estimation of Mulliken atomic charges using the DFT/B3LYP method with a 6-31G** basis set in the gaseous phase contributes valuable information to the understanding of the electronic characteristics of the studied compounds. These data serve as a foundation for elucidating the reactivity patterns of compounds, guiding future research endeavors, and informing applications in various scientific disciplines. The geometrical parameters of the anti-ZIKV biological Compounds 1, 2, and 3 are calculated using the Density function B3LYP/6-31G** basis set. Optimized parameters (bond length, bond angle, *etc.*) have been used for the computations of electronic structure properties and IR frequencies. MEP, Mulliken charge, and HOMO-LUMO analyses show that the compounds are chemically active. The most sensitive region of the molecules is predicted by MEP. The charge transfer interaction inside the molecule is supported by the difference in HOMO and LUMO energy. Global reactivity descriptors have been used to determine the chemical reactivity and site selectivity of compounds. Several experimental vaccines are undergoing early human clinical testing and could be created as a treatment candidate for the treatment of ZIKV. The docking analysis of the molecules within the MTase enzyme binding site reveals that Afatinib and Compound 3 exhibit higher binding affinities compared to Compound 1 and Compound 2. Molecular dynamics simulations of the top-ranked complexes (Afatinib@MTase and Compound 3@MTase) further confirm their stability within the Zika virus MTase binding site, highlighting their potential as promising candidates for the development of anti-Zika virus therapeutics.

Acknowledgements

The authors thank the Center for Development of Advanced Computing (CDAC), Pune, for providing a high-performance supercomputing facility.

Disclosure statement

Conflict of interest: The authors declare that they have no conflict of interest.
Ethical approval: All ethical guidelines have been followed.

CRediT authorship contribution statement

Conceptualization: Umesh Yadava; Methodology: Umesh Yadava; Software: Umesh Yadava; Validation: Umesh Yadava, Akhilesh Kumar Rao; Formal Analysis: Umesh Yadava, Akhilesh Kumar Rao; Investigation: Umesh Yadava, Akhilesh Kumar Rao; Resources: Umesh Yadava; Data Curation: Umesh Yadava, Akhilesh Kumar Rao; Writing - Original Draft: Umesh Yadava, Akhilesh Kumar Rao; Writing - Review and Editing: Umesh Yadava; Visualization: Akhilesh Kumar Rao; Funding acquisition: Umesh Yadava, Akhilesh Kumar Rao; Supervision: Umesh Yadava; Project Administration: Umesh Yadava.

Funding

Umesh Yadava thanks Council of Science and Technology, Uttar Pradesh, Lucknow, India for funding through its major research project.

ORCID and Email

Akhilesh Kumar Rao
akhileshkrao@rediffmail.com
https://orcid.org/0009-0003-8523-8535
Umesh Yadava
u_yadava@yahoo.com
umesh.phy@ddugu.ac.in
https://orcid.org/0000-0002-9127-532X

References

[1]. Ledermann, J. P.; Guillaumot, L.; Yug, L.; Saweyog, S. C.; Tided, M.; Machieng, P.; Pretrick, M.; Marfel, M.; Griggs, A.; Bel, M.; Duffy, M. R.; Hancock, W. T.; Ho-Chen, T.; Powers, A. M. Aedes hensilli as a Potential Vector of Chikungunya and Zika Viruses. *PLoS Negl Trop Dis* **2014**, *8* (10), e3188.

[2]. Altaf Khan, M.; Farhan, M.; Islam, S.; Bonyah, E. Modeling the transmission dynamics of avian influenza with saturation and psychological effect. *Discrete amp; Contin. Dyn. Syst. - S* **2019**, *12* (3), 455–474.

[3]. Newman, C.; Friedrich, T. C.; O'Connor, D. H. Macaque monkeys in Zika virus research: 1947–present. *Curr. Opin. Virol.* **2017**, *25*, 34–40.

[4]. Charrel, R. N.; Leparc-Goffart, I.; Pas, S.; de Lamballerie, X.; Koopmans, M.; Reusken, C. Background review for diagnostic test development for Zika virus infection. *Bull. World Health Organ.* **2016**, *94* (8), 574–584D.

[5]. Singh, S.; Farr, D.; Kumar, A. Ocular Manifestations of Emerging Flaviviruses and the Blood-Retinal Barrier. *Viruses* **2018**, *10* (10), 530.

[6]. Balmaseda, A.; Stettler, K.; Medialdea-Carrera, R.; Collado, D.; Jin, X.; Zambrana, J. V.; Jaconi, S.; Cameroni, E.; Saborio, S.; Rovida, F.; Percivalle, E.; Ijaz, S.; Dicks, S.; Ushiro-Lumb, I.; Barzon, L.; Siqueira, P.; Brown, D. W.; Baldanti, F.; Tedder, R.; Zambon, M.; de Filippis, A. M.; Harris, E.; Corti, D. Antibody-based assay discriminates Zika virus infection from other flaviviruses. *Proc. Natl. Acad. Sci. U.S.A.* **2017**, *114* (31), 8384–8389.

[7]. Saeed, P. A.; Shilpa, R.; Sujith, A. A water-mediated approach for the preparation of conductive poly(3,4-ethylenedioxythiophene)-decorated poly(methyl methacrylate) microcomposites. *Mater. Adv.* **2022**, *3* (9), 3875–3884.

[8]. Tilak, R.; Ray, S.; Tilak, V.; Mukherji, S. Dengue, chikungunya … and the missing entity – Zika fever: A new emerging threat. *Med. J. Armed Forces India* **2016**, *72* (2), 157–163.

[9]. Waafira, A.; Subbaram, K.; Faiz, R.; Un Naher, Z.; Manandhar, P. L.; Ali, S. Zika virus outbreak are on the rise in India: Clinical features, complications and prevention. *New Microbes New Infect.* **2024**, *62*, 101493.

[10]. Petersen, E.; Wilson, M. E.; Touch, S.; McCloskey, B.; Mwaba, P.; Bates, M.; Dar, O.; Mattes, F.; Kidd, M.; Ippolito, G.; Azhar, E. I.; Zumla, A. Rapid Spread of Zika Virus in The Americas - Implications for Public Health Preparedness for Mass Gatherings at the 2016 Brazil Olympic Games. *Int. J. Infect. Dis.* **2016**, *44*, 11–15.

[11]. Noronha, L. d.; Zanluca, C.; Azevedo, M. L.; Luz, K. G.; Santos, C. N. Zika virus damages the human placental barrier and presents marked fetal neurotropism. *Mem. Inst. Oswaldo Cruz* **2016**, *111* (5), 287–293.

[12]. Jiang, X.; Loeb, J. C.; Manzanas, C.; Lednicky, J. A.; Fan, Z. H. Valve-Enabled Sample Preparation and RNA Amplification in a Coffee Mug for Zika Virus Detection. *Angew Chem Int Ed* **2018**, *57* (52), 17211–17214.

[13]. Gupta, G.; Shah, Y.; Poudel, A.; Pun, R.; Pant, K.; Kshetri, R.; Pandey, K.; Pandey, B. Serological and Molecular Study of Dengue Viruses in Different Hospitals of Nepal. *Nep J. Med Sci* **2013**, *2* (1), 20–25.

[14]. Noorbakhsh, F.; Abdolmohammadi, K.; Fatahi, Y.; Dalili, H.; Rasoolinejad, M.; Rezaei, F.; Salehi-Vaziri, M.; Shafiei-Jandaghi, N. Z.; Gooshki, E. S.; Zaim, M.; Nicknam, M. H. Zika virus infection, basic and clinical aspects: A review article. *Iran. J. Public Health* **2019**, *48*, 20–31.

[15]. Bharadwaj, S.; Rao, A. K.; Dwivedi, V. D.; Mishra, S. K.; Yadava, U. Structure-based screening and validation of bioactive compounds as Zika virus methyltransferase (MTase) inhibitors through first-principle density functional theory, classical molecular simulation and QM/MM affinity estimation. *J. Biomol. Struct. Dyn.* **2020**, *39* (7), 2338–2351.

[16]. Kurosaki, Y.; Martins, D. B.; Kimura, M.; Catena, A. d.; Borba, M. A.; Mattos, S. d.; Abe, H.; Yoshikawa, R.; de Lima Filho, J. L.; Yasuda, J. Development and evaluation of a rapid molecular diagnostic test for Zika virus infection by reverse transcription loop-mediated isothermal amplification. *Sci Rep* **2017**, *7* (1), 13503 https://doi.org/10.1038/s41598–017–13836–9.

[17]. L'Huillier, A. G.; Lombos, E.; Tang, E.; Perusini, S.; Eshaghi, A.; Nagra, S.; Frantz, C.; Olsha, R.; Kristjanson, E.; Dimitrova, K.; Safronetz, D.; Drebot, M.; Gubbay, J. B. Evaluation of Altona Diagnostics RealStar Zika Virus Reverse Transcription-PCR Test Kit for Zika Virus PCR Testing. *J. Clin Microbiol* **2017**, *55* (5), 1576–1584.

[18]. Quanquin, N.; Wang, L.; Cheng, G. Potential for treatment and a Zika virus vaccine. *Curr. Opin. Pediatr.* **2017**, *29* (1), 114–121.

[19]. Yadava, U.; Gupta, D. K.; Roychoudhury, M. Theoretical investigations on molecular structure and IR frequencies of 4-n-nonyl-4′-cyanobiphenyl in light of experimental results. *J. Mol. Liq.* **2010**, *156* (2-3), 187–190.

[20]. Shukla, B. K.; Yadava, U.; Roychoudhury, M. Theoretical explorations on the molecular structure and IR frequencies of 3-phenyl-1-tosyl-1H-pyrazolo[3,4-d]pyrimidin-4-amine in view of experimental results. *J. Mol. Liq.* **2015**, *212*, 325–330.

[21]. Chattaraj, P. K.; Poddar, A. Molecular Reactivity in the Ground and Excited Electronic States through Density-Dependent Local and Global Reactivity Parameters. *J. Phys. Chem. A.* **1999**, *103* (43), 8691–8699.

[22]. Yadava, U.; Gupta, H.; Roychoudhury, M. A comparison of crystallographic and DFT optimized geometries on two taxane diterpenoids and docking studies with phospholipase A2. *Med Chem Res* **2011**, *21* (9), 2162–2168.

[23]. Zakaria, M. K.; Carletti, T.; Marcello, A. Cellular Targets for the Treatment of Flavivirus Infections. *Front. Cell. Infect. Microbiol.* **2018**, *8*, 398 https://doi.org/10.3389/fcimb.2018.00398.

[24]. Chuang, F.; Liao, C.; Hu, M.; Chiu, Y.; Lee, A.; Huang, S.; Chiu, Y.; Tsai, P.; Su, B.; Chang, T.; Lin, C.; Shih, C.; Yen, L. Antiviral Activity of Compound L3 against Dengue and Zika Viruses In Vitro and In Vivo. *International Journal of Molecular Sciences, IJMS.* **2020**, *21* (11), 4050.

[25]. Tirado-Rives, J.; Jorgensen, W. L. Performance of B3LYP density functional methods for a large set of organic molecules. *J. Chem. Theory Comput.* **2008**, *4*, 2, 297–306.

[26]. Rassolov, V. A.; Ratner, M. A.; Pople, J. A.; Redfern, P. C.; Curtiss, L. A. 6-31G* basis set for third-row atoms. *J. Comput Chem* **2001**, *22* (9), 976–984.

[27]. Frisch, M. J.; Trucks, G. W.; Schlegel, H. B.; Scuseria, G. E.; Robb, M. A.; Cheeseman, J. R.; Montgomery, J. A.; Vreven, T.; Kudin, K. N.; Burant, J. C.; Millam, J. M.; Iyengar, S. S.; Tomasi, J.; Barone, V.; Mennucci, B.; Cossi, M.; Scalmani, G.; Rega, N.; Petersson, G. A.; Nakatsuji, H.; Hada, M.; Ehara, M.; Toyota, K.; Fukuda, R.; Hasegawa, J.; Ishida, M.; Nakajima, T.; Honda, Y.; Kitao, O.; Nakai, H.; Klene, M.; Li, X.; Knox, J. E.; Hratchian, H. P.; Cross, J. B.; Adamo, C.; Jaramillo, J.; Gomperts, R.; Stratmann, R. E.; Yazyev, O.; Austin, A. J.; Cammi, R.; Pomelli, C.; Ochterski, J. W.; Ayala, P. Y.; Morokuma, K.; Voth, G. A.; Salvador, P.; Dannenberg, J. J.; Zakrzewski, V. G.; Dapprich, S.; Daniels, A. D.; Strain, M. C.; Farkas, O.; Malick, D. K.; Rabuck, A. D.; Raghavachari, K; Foresman, J. B.; Ortiz, J. V.; Cui, Q.; Baboul, A. G.; Clifford, S.; Cioslowski, J.; Stefanov, B. B.; Liu, G.; Liashenko, A.; Piskorz, P.; Komaromi, I.; Martin, R. L.; Fox, D. J.; Keith, T.; Al-Laham, M. A.; Peng, C. Y.; Nanayakkara, A.; Challacombe, M.; Gill, P. M. W.; Johnson, B.; Chen, W.; Wong, M. W.; Gonzalez, C.; Pople, J. A. Gaussian, Inc., Wallingford CT, 2004.

[28]. Yadava, U.; Singh, M.; Roychoudhury, M. Gas-phase conformational and intramolecular π–π interaction studies on some pyrazolo[3,4-d]pyrimidine derivatives. *Comput. Theor. Chem.* **2011**, *977*, 134–139.

[29]. Bharadwaj, S.; Dubey, A.; Kamboj, N. K.; Sahoo, A. K.; Kang, S. G.; Yadava, U. Drug repurposing for ligand-induced rearrangement of Sirt2 active site-based inhibitors via molecular modeling and quantum mechanics calculations. *Sci Rep* **2021**, *11* (1), https://doi.org/10.1038/s41598–021–89627–0.

[30]. Yadava, U.; Singh, M.; Roychoudhury, M. Pyrazolo[3,4-d]pyrimidines as inhibitor of anti-coagulation and inflammation activities of phospholipase A 2 : insight from molecular docking studies. *J. Biol Phys* **2013**, *39* (3), 419–438.

[31]. Glide: Version 5.8 Schrödinger, LLC, New York (2012).

[32]. DESMOND Molecular Dynamics System, version 3.1, D. E. Shaw Research, New York, NY (2012).

[33]. Bowers, K. J.; Chow, D. E.; Xu, H.; Dror, R. O.; Eastwood, M. P.; Gregersen, B. A.; Klepeis, J. L.; Kolossvary, I.; Moraes, M. A.; Sacerdoti, F. D.; Salmon, J. K.; Shan, Y.; Shaw, D. E. Scalable algorithms for molecular dynamics simulations on commodity clusters. In ACM/IEEE SC 2006 Conference (SC'06); IEEE, 2006; pp. 43–43.
[34]. Yadava, U.; Yadav, V. K.; Yadav, R. K. Novel anti-tubulin agents from plant and marine origins: insight from a molecular modeling and dynamics study. *RSC Adv.* **2017**, *7*, 15917–15925.
[35]. Mark, P.; Nilsson, L. Structure and dynamics of the TIP3P, SPC, and SPC/E water models at 298 K. *J. Phys. Chem. A* **2001**, *105*, 9954–9960.
[36]. Singh, A.; Yadav, R. K.; Shati, A.; Kamboj, N. K.; Hasssan, H.; Bharadwaj, S.; Rana, R.; Yadava, U. Understanding the self-assembly dynamics of A/T absent "four-way DNA junctions with sticky ends" at altered physiological conditions through molecular dynamics simulations. *PLoS One* **2023**, *18*, e0278755.
[37]. Mulliken, R. S. Electronic population analysis on LCAO-MO molecular wave functions. III. Effects of hybridization on overlap and gross AO populations. *J. Chem. Phys.* **1955**, *23*, 2338–2342.
[38]. Elshakre, M. E.; Noamaan, M. A.; Moustafa, H.; Butt, H. Density Functional Theory, chemical reactivity, pharmacological potential and molecular docking of dihydrothiouracil-indenopyridopyrimidines with human-DNA topoisomerase II. *Int. J. Mol. Sci.* **2020**, *21*, 1253.
[39]. Yu, J.; Su, N. Q.; Yang, W. Describing chemical reactivity with frontier molecular orbitalets. *JACS Au* **2022**, *2*, 1383–1394.
[40]. Yadav, G.; Yadava, U. Exploring the electronic structure and interaction mechanism of nucleic acid bases on pristine graphene and beryllium-oxide-graphene layers. *Comput. Theor. Chem.* **2024**, *1239*, 114787.
[41]. Gadre, S. R.; Suresh, C. H.; Mohan, N. Electrostatic Potential Topology for Probing Molecular Structure, Bonding and Reactivity. *Molecules* **2021**, *26* (11), 3289.
[42]. Kushwaha, Y.; Yadava, U. DFT investigation on the effect of asymmetry on electro-optical properties of bent-core liquid crystals. *Ph. Transit.* **2025**, *98* (1), 55–71.
[43]. Parr, R. G.; Pearson, R. G. Absolute hardness: companion parameter to absolute electronegativity. *J. Am. Chem. Soc.* **1983**, *105*, 7512–7516.
[44]. Lu, C.; Wu, C.; Ghoreishi, D.; Chen, W.; Wang, L.; Damm, W.; Ross, G. A.; Dahlgren, M. K.; Russell, E.; Von Bargen, C. D.; Abel, R.; Friesner, R. A.; Harder, E. D. OPLS4: Improving force field accuracy on challenging regimes of chemical space. *J. Chem. Theory Comput.* **2021**, *17*, 4291–4300.